Supplemental Data

Kinetic Parameter Estimation

The impulse response function of the adiabatic approximation to the tissue homogeneity (AATH) model (*17*) can be written in terms of Heaviside step functions, $H(t-a)=\begin{cases}1 & t \geq a \\ 0 & t < a\end{cases}$:

$$R^{AATH}(t) = F[H(t) - H(t-T_c)] + K_1 e^{-k_2(t-T_c)} H(t-T_c). \quad \text{(S1)}$$

Substituting the above form of $R^{AATH}(t)$ into Equation (4) results in a parametric form of the AATH time-activity curve:

$$\begin{aligned} Q^{AATH}(t) = F\left[\int_{t_d}^{t} C_{wb}(\tau - t_d)\, d\tau - \int_{t_d+T_c}^{t} C_{wb}(\tau - t_d - T_c)\, d\tau\right] \\ + K_1 \int_{t_d+T_c}^{t} C_p(\tau - t_d - T_c) e^{-k_2(t-\tau)} H(t-\tau)\, d\tau \end{aligned} \quad \text{(S2)}$$

where $C_{wb}(t)$ and $C_p(t)$ are the whole-blood and plasma arterial input functions, respectively, and account for whole-blood flow whereas tracer exchange occurs in plasma. Each integral is zero when t is less than its respective lower limit of integration. Similarly, the impulse response function of the standard one-tissue compartment model (S1TC) can be expressed:

$$R^{S1TC}(t) = v_b \delta(t) + K_1 e^{-k_2 t} \quad \text{(S3)}$$

where $\delta(t)$ is the Dirac delta function. The parametric form is then:

$$Q^{S1TC}(t) = v_b C_{wb}(t - t_d) + K_1 \int_{t_d}^{t} C_p(\tau - t_d) e^{-k_2(t-\tau)}\, d\tau \quad \text{(S4)}$$

We interpreted the $C_{wb}(t)$ terms as the intravascular distributions of the S1TC and AATH fitted time-activity curves, and the $C_p(t)$ term as the extravascular tissue distribution. Of note, it can be shown that $R^{S1TC}(t)$ is a special case of $R^{AATH}(t)$ when $T_c \approx 0$. Substituting $F = v_b/T_c$ in Equation (S1) and taking the limit as T_c approaches zero:

$$\lim_{T_c \to 0} R^{AATH}(t) = \lim_{T_c \to 0} \left(\frac{v_b}{T_c} [H(t) - H(t-T_c)] + K_1 e^{-k_2(t-T_c)} H(t-T_c) \right)$$

The first term of the limit can be recognized as the derivative of the Heaviside step function, which is the Dirac delta function. Therefore,

$$\lim_{T_c \to 0} R^{AATH}(t) = v_b \delta(t) + K_1 e^{-k_2 t} = R^{S1TC}(t) \quad \text{(S5)}$$

In this work, we follow the notation used in distributed kinetic models (*16*,*17*) and dynamic contrast-enhanced MRI and CT kinetic modeling conventions (*30*,*31*) where the tissue fraction $(1 - v_b)$ has been absorbed into K_1. Time-activity curve fitting is not affected but our reported F and K_1 values are given per unit voxel volume rather than tissue volume.

All kinetic parameters are estimated using the least-square curve fitting formulation

$$\boldsymbol{\theta} = \underset{\boldsymbol{\theta}}{\operatorname{argmin}} \sum_{m=1}^{M} w_m \left(Q(t_m) - \hat{Q}(t_m) \right)^2 \quad \text{(S6)}$$

where $\boldsymbol{\theta}$ includes all unknown kinetics parameters, $Q(t)$ and $\hat{Q}(t)$ are the measured and fitted time-activity curves, respectively, M is the number of frames, t_m is the midpoint time of the mth frame, and w_m is the weighting factor. In this work, we used $w_m = 1$.

We used a basis function method (*28*,*29*) for solving the least-square fitting problem in Equation (S6) to estimate all kinetic parameters, including time delay, on time-activity curves of the dynamic scan's first two minutes. For the AATH model, basis functions were computed by using grid searched values of t_d from 0 to 50 s, T_c from 3 to 50 s, and 100 logarithmically spaced values of k_2 between 6×10^{-4} to 15 min^{-1}. The remaining linear parameters (F, K_1) were then estimated by a non-negative linear least squares algorithm (*32*). The final set of parameters (t_d, T_c, F, K_1, k_2) were the ones that produced the least squared differences between the measured and fitted time-activity curves. A similar procedure was followed for the S1TC model but without T_c in the grid search and linearly estimating v_b and K_1.

For both radiotracers, we assumed that whole-blood tracer activity was equal to that in blood plasma over the first two minutes of the dynamic PET scan. ^{11}C-butanol rapidly equilibrates uniformly between blood plasma and erythrocytes (*33*) and for ^{18}F-FDG, blood plasma is commonly approximated by the whole-blood image-derived arterial input function. This approximation may result in a small bias in K_1 estimates but otherwise should not affect blood flow or curve fitting.

The quality of the AATH and S1TC model time-activity curve fits were compared using the Akaike information criterion (AIC) (*43*):

$$AIC = M \ln \frac{\sum_{m=1}^{M} \left(Q(t_m) - \hat{Q}(t_m) \right)^2}{M} + 2n + \frac{2n(n+1)}{M - n - 1} \quad \text{(S7)}$$

where n is the number of model parameters. The AATH model comprised n = 5 parameters (t_d, T_c, F, K_1, k_2) while the S1TC had n = 4 (t_d, v_b, K_1, k_2).

Tissue Segmentation

The lungs, renal cortex, spleen, and skeletal muscle (splenius capitis, psoas, thigh, calves), and bone marrow in the pelvis and lumbar vertebrae were manually delineated on 3D Slicer (Version 5.2) (*36*) by referencing a combination of the total-body CT, dynamic PET, and 0-2 minute static PET images. For the brain, we used a deep learning-based ^{18}F-FDG-PET/CT segmentation tool (*37*) to delineate the 83 brain regions of the Hammersmith atlas (*38*), which were grouped to form masks of the cortical and subcortical grey matter, white matter, brainstem, and whole cerebellum. The grey and white matter in the cerebrum were distinguished by an Otsu threshold (*39*). In participants with both ^{18}F-FDG and ^{11}C-butanol PET, FDG brain masks were resampled to the ^{11}C-butanol-PET brain space by co-registering (*40*) the 0-2 minute static ^{18}F-FDG-PET brain image to that of the ^{11}C-butanol PET. Segmentations were visually inspected and manually adjusted as needed to avoid large vessels and organ boundaries where motion and spillover were more prevalent.

Supplemental Table 1. Range of average blood flow and mean vascular transit time values reported in literature, mainly for healthy individuals

Tissue	Blood Flow [mL/min/cm^3]		Mean Vascular Transit Time [s]	
	Literature Range	References	Literature Range	References
Grey Matter	0.44–0.83	(*4*,*6*,*18*,*45*–*47*)*	2.8–5.5	(*45*,*59*)*,**
White Matter	0.16–0.32	(*4*,*6*,*18*,*45*,*47*)*	3.5–7.1	(*45*,*59*)*,**
Cerebellum	0.41–0.56	(*45*,*48*,*49*)*	3.3–5.7	(*45*,*59*)*,**
Brainstem	0.31	(*50*)**	N/A	
Bone Marrow	0.10–0.18	(*4*,*51*)*	35.3	(*60*)**
Skeletal Muscle	0.03–0.05	(*4*,*52*)*	40.8	(*61*)**
Spleen	1.3–1.7	(*4*,*53*,*54*)*	8.1–10.7	(*62*,*63*)***
Renal Cortex	1.6–2.0	(*4*,*55*)*	6.6–7.4	(*64*,*65*)**
Lungs	1.2–1.7	(*4*,*56*–*58*)*	4.7	(*66*)**

* PET ** MR perfusion *** CT perfusion

Supplemental Table 2. Practical identifiability analysis of the adiabatic approximation to the tissue homogeneity (AATH) model

Tissue / Parameter	Noise Scale (*27*)	Mean (Standard Deviation) Error [%]				
		Blood Flow	K_1	E	v_b	T_c
Cortical GM	2.4	-0.6 (3.3)	0.1 (0.8)	0.9 (3.5)	0.0 (1.4)	0.9 (4.5)
Subcortical GM	11.8	-3.7 (12.6)	-0.5 (2.9)	6.1 (14.7)	2.9 (7.7)	12.0 (25.2)
White Matter	4.1	0.7 (6.1)	0 (1.9)	-0.2 (5.5)	0.0 (4.0)	0.1 (8.8)
Cerebellum	3.3	-0.3 (5.3)	0.0 (1.3)	0.6 (5.1)	0.2 (2.6)	1.0 (7.3)
Brainstem	10.0	0.6 (14.2)	-0.3 (3.4)	1.3 (13.3)	1.3 (8.5)	4.2 (21.8)
Bone Marrow	3.2	2.5 (4.2)	-1.3 (5.5)	-3.5 (4.6)	3.0 (21.8)	3.1 (23.6)
Skeletal Muscle	4.7	6.4 (8.7)	0.8 (6.7)	-4.4 (7.3)	4.8 (50.9)	3.6 (53.2)
Spleen	14.6	-0.8 (8.3)	-2.6 (9.1)	-1.4 (8.6)	11.6 (23.2)	15.8 (33.0)
Renal Cortex	15.3	0.4 (4.3)	0.2 (5.5)	-0.1 (5.9)	-0.1 (3.4)	-0.2 (6.2)
Lungs	7.1	0.0 (2.7)	1.3 (11.0)	1.4 (11.3)	0.0 (1.4)	0.1 (2.5)

A negative error indicates that the predicted value underestimated the true value. K_1 indicates the blood-to-tissue transport rate; E, extraction fraction; v_b, blood volume; T_c, mean vascular transit time; GM, grey matter

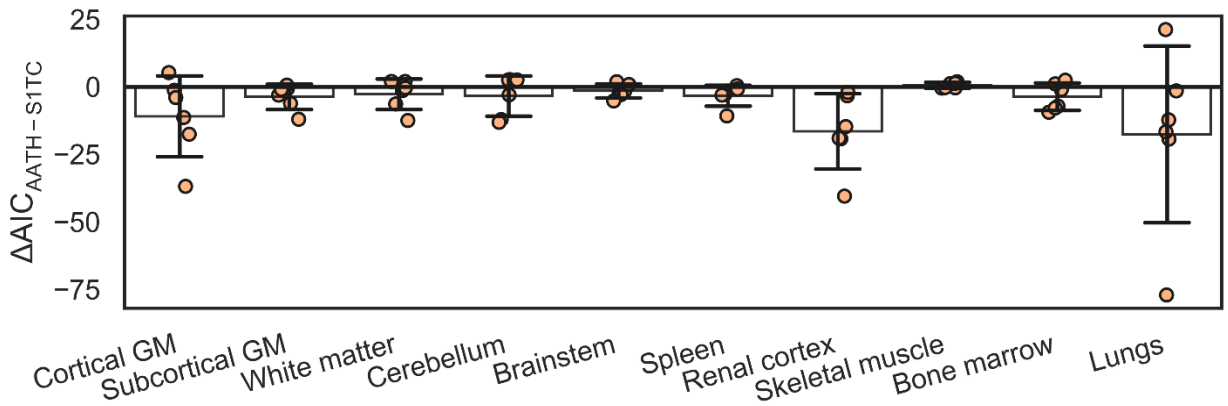

Supplemental Figure 1. Difference in the Akaike Information Criterion (AIC) between the adiabatic approximation to the tissue homogeneity (AATH) and standard one-tissue compartment (S1TC) models for high-temporal resolution (60×1 s, 30×2 s) ^{11}C-Butanol regional time-activity curves. A negative AIC indicates a preference towards the AATH model. GM indicates grey matter.

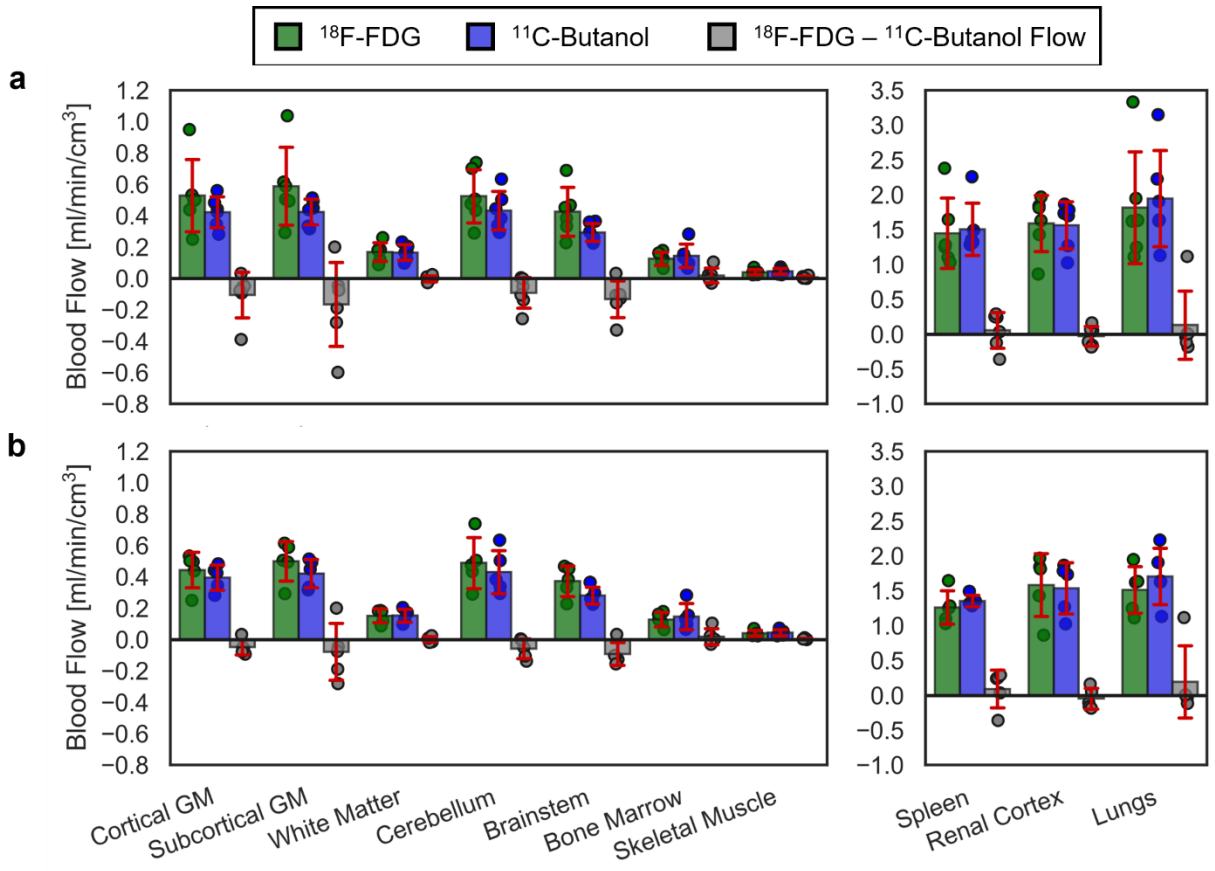

Supplemental Figure 2. Regional blood flow comparisons between our proposed ^{18}F-FDG method and the ^{11}C-butanol reference in six participants scanned with both radiotracers. (a) Including all six participants and (b) excluding the participant shown in Supplemental Figure 4.

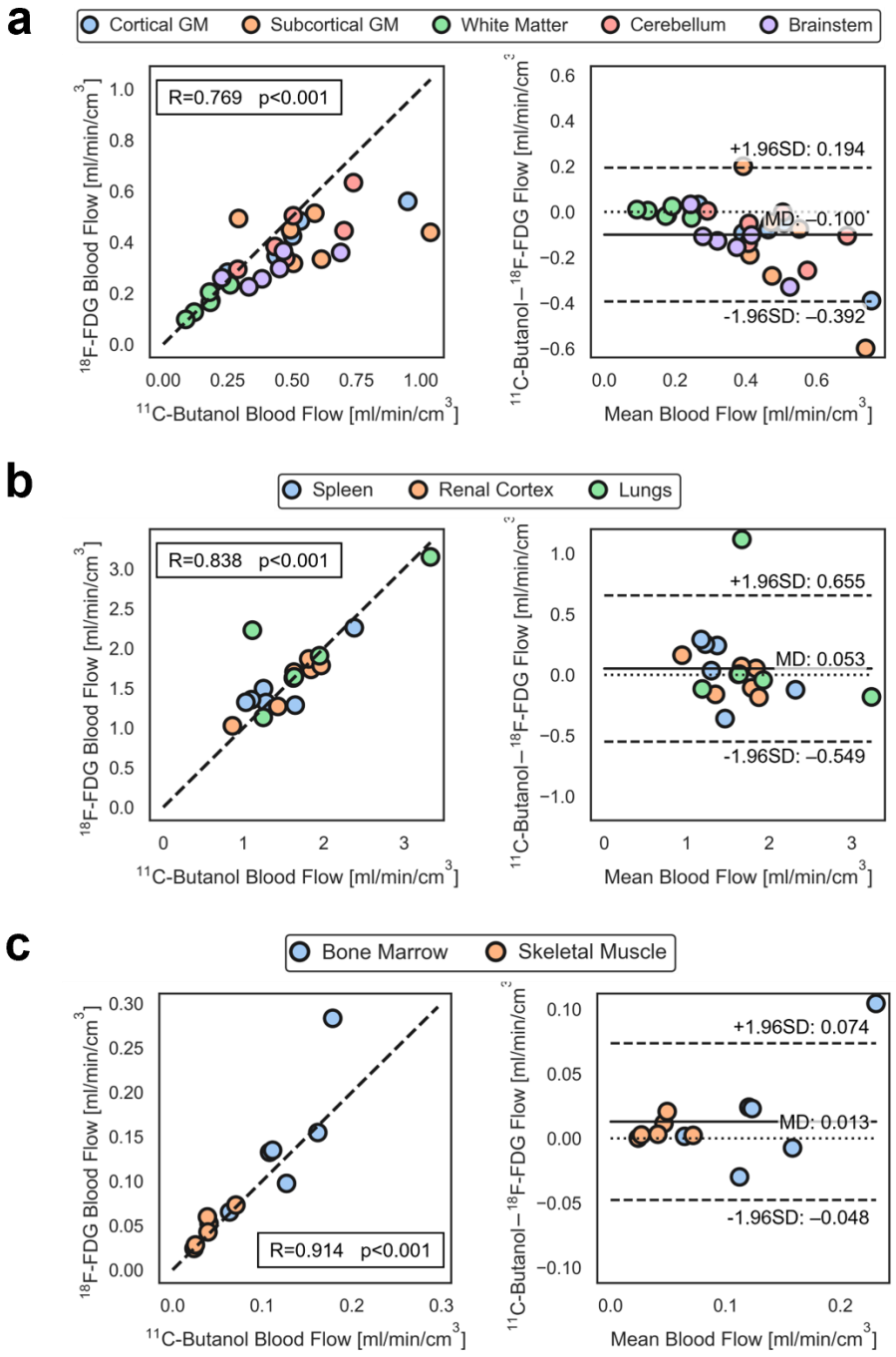

Supplemental Figure 3. Correlation (left) and Bland-Altman (right) plots comparing ^{18}F-fluorodeoxyglucose (FDG) blood flow with our proposed method against ^{11}C-butanol reference in the same subjects and stratified by (a) brain regions, (b) high blood flow tissues, and (c) low blood flow tissue. MD indicates mean difference; SD, standard deviation.

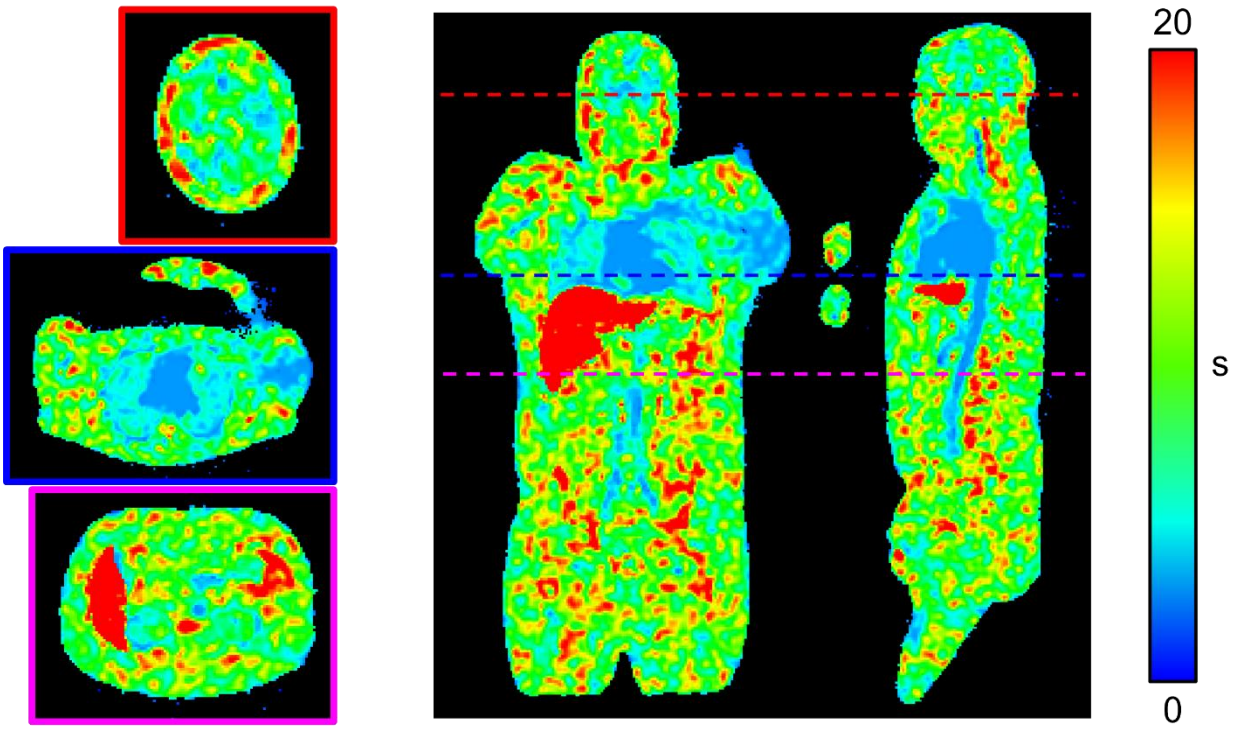

Supplemental Figure 4. Representative parametric image of the mean vascular transit time, T_c (units: seconds), from a healthy volunteer scanned with total-body dynamic ^{18}F-FDG PET. Note that T_c is low in large blood pools like the aorta, cardiac chambers, and cerebral arteries because of the high blood flow rates in the arterial system. A near-constant value is seen at the blood pools because the minimum T_c allowed in the parameter estimation algorithm was 3 s based on the used frame rate. Our work did not correct for spillover in the myocardium and as such there is poor contrast of this structure versus adjacent blood pools.

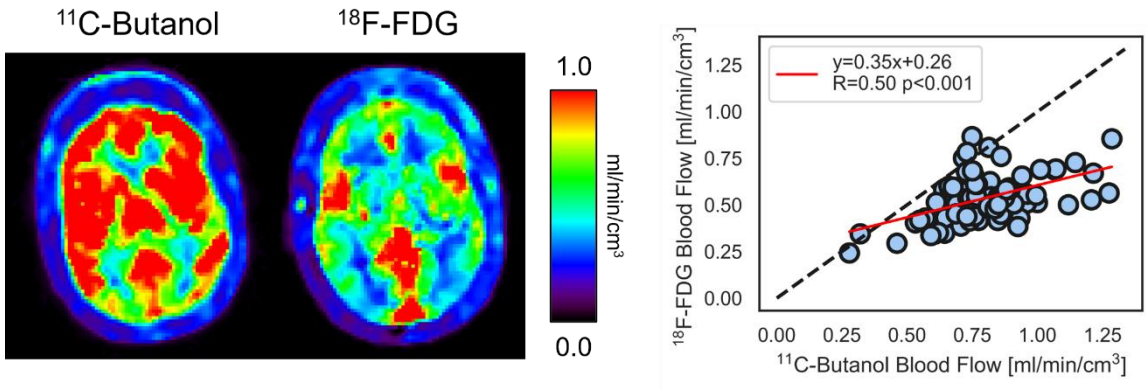

Supplemental Figure 5. ^{11}C-butanol and ^{18}F-FDG cerebral blood flow parametric images showed substantial differences in one participant scanned with both radiotracers. The correlation plot compares blood flow estimated with ^{11}C-butanol and ^{18}F-FDG across the 83 Hammersmith brain atlas regions.[7] This participant self-reported having claustrophobia. Claustrophobia and anxiety (*67*,*68*) among other physiological and methodological factors may have contributed to this discrepancy and thus warrants a future test-retest study.

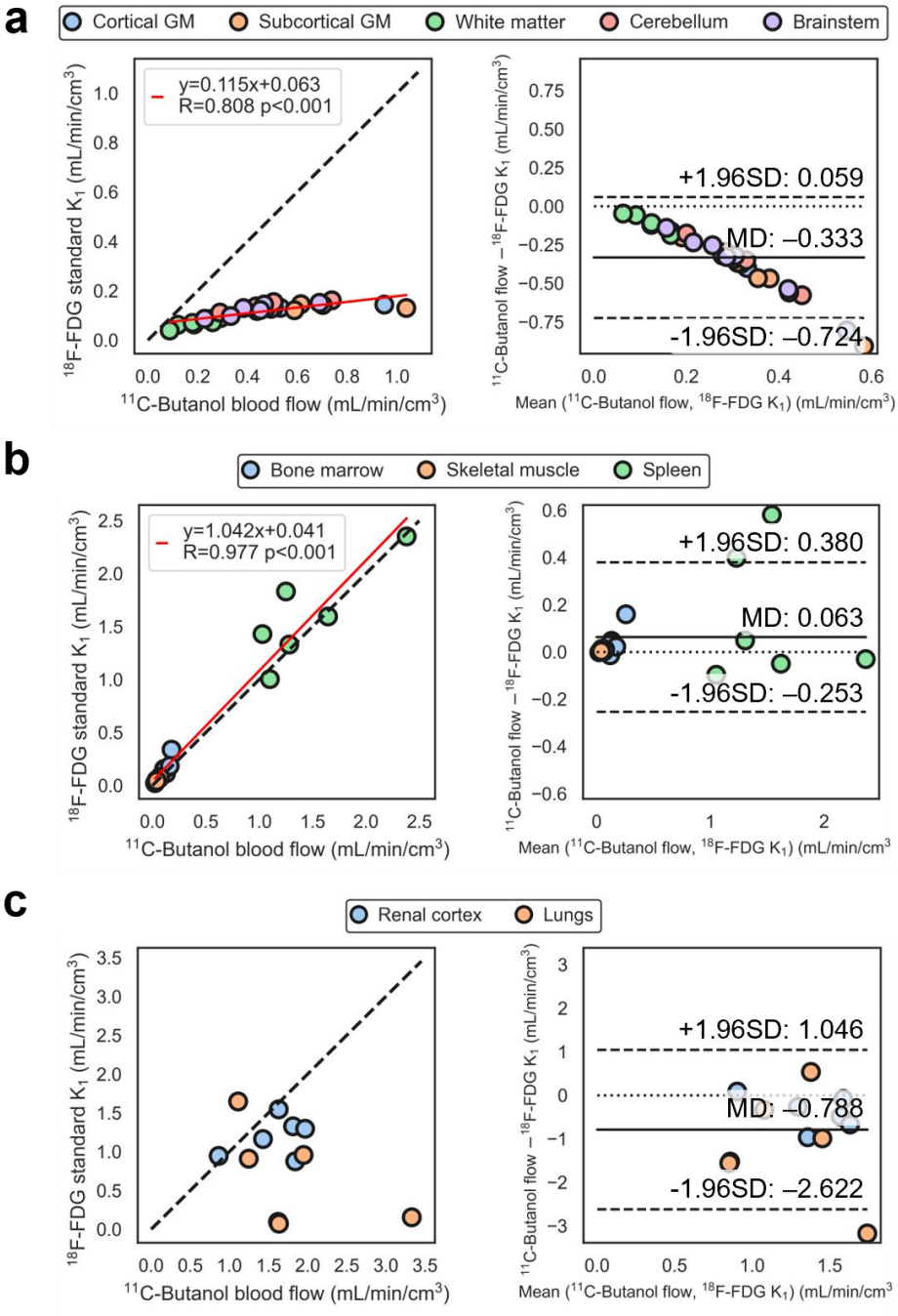

Supplemental Figure 6. Correlation (left) and Bland-Altman (right) plots comparing ^{11}C-butanol blood flow and ^{18}F-fluorodeoxyglucose (FDG) standard one-tissue compartment (S1TC) model K_1. Plots are stratified by (a) brain, (b) high extraction fraction, and (c) low to moderate extraction fraction (Table 1).

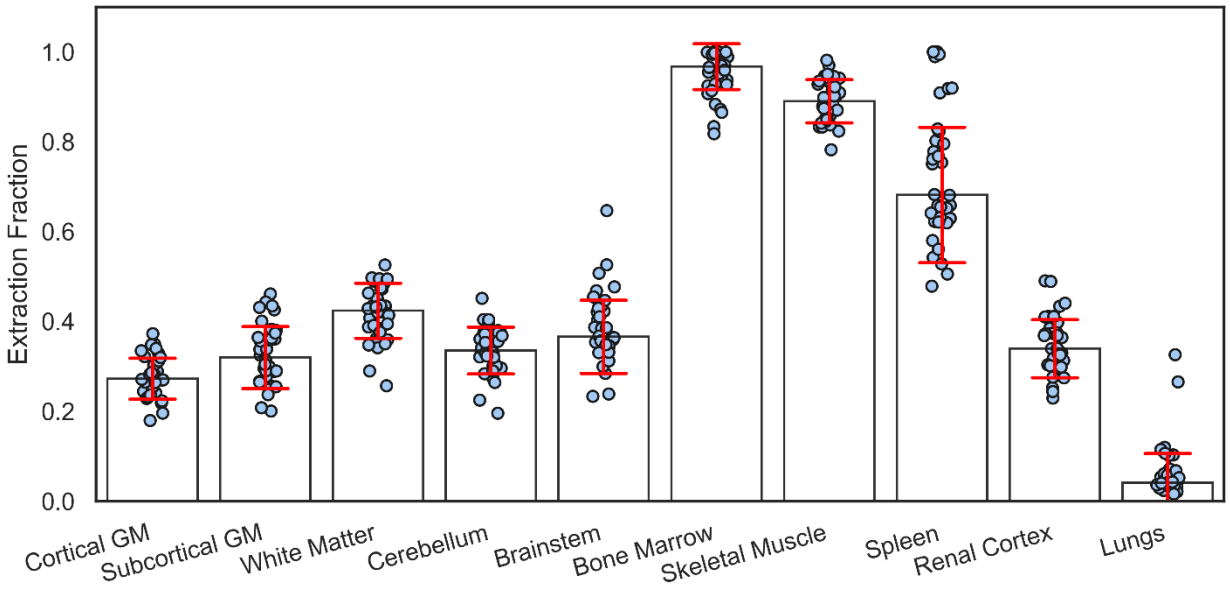

Supplemental Figure 7. Regional ^{18}F-fluorodeoxyglucose (FDG) extraction fractions estimated with the proposed method.

Supplemental References (indexed from main text)

4. Li EJ, López JE, Spencer BA, et al. Total-Body Perfusion Imaging with [11C]-Butanol. *J Nucl Med*. 2023;64:1831-1838.

6. Herscovitch P, Raichle ME, Kilbourn MR, Welch MJ. Positron Emission Tomographic Measurement of Cerebral Blood Flow and Permeability—Surface Area Product of Water Using [^{15}O]Water and [^{11}C]Butanol. *J Cereb Blood Flow Metab*. 1987;7:527-542.

16. Larson KB, Markham J, Raichle ME. Tracer-Kinetic Models for Measuring Cerebral Blood Flow Using Externally Detected Radiotracers. *J Cereb Blood Flow Metab*. 1987;7:443-463.

17. St Lawrence KS, Lee T-Y. An Adiabatic Approximation to the Tissue Homogeneity Model for Water Exchange in the Brain: I. Theoretical Derivation. *J Cereb Blood Flow Metab*. 1998;18:1365-1377.

18. Quarles RP, Mintun MA, Larson KB, Markham J, MacLeod AM, Raichle ME. Measurement of Regional Cerebral Blood Flow with Positron Emission Tomography: A Comparison of [^{15}O]Water to [^{11}C]Butanol with Distributed-Parameter and Compartmental Models. *J Cereb Blood Flow Metab*. 1993;13:733-747.

27. Zuo Y, Sarkar S, Corwin MT, Olson K, Badawi RD, Wang G. Structural and practical identifiability of dual-input kinetic modeling in dynamic PET of liver inflammation. *Phys Med Biol*. 2019;64:175023.

28. Chung KJ, Abdelhafez YG, Spencer BA, et al. Quantitative PET imaging and modeling of molecular blood-brain barrier permeability. *medRxiv*. July 2024.

29. Gunn RN, Lammertsma AA, Hume SP, Cunningham VJ. Parametric Imaging of Ligand-Receptor Binding in PET Using a Simplified Reference Region Model. *NeuroImage*. 1997;6:279-287.

30. Sourbron SP, Buckley DL. Tracer kinetic modelling in MRI: estimating perfusion and capillary permeability. *Phys Med Biol*. 2012;57:R1-R33.

31. Chung KJ, De Sarno D, Lee T-Y. Quantitative functional imaging with CT perfusion: technical considerations, kinetic modeling, and applications. *Front Phys*. 2023;11:1246973.

32. Lawson CL, Hanson RJ. Solving least squares problems. Philadelphia: SIAM; 1995.

33. Knapp WolframH, Helus F, Oberdorfer F, et al. 11C-Butanol for imaging of the blood-flow distribution in tumor-bearing animals. *Eur J Nucl Med*. 1985;10-10.

36. Fedorov A, Beichel R, Kalpathy-Cramer J, et al. 3D Slicer as an image computing platform for the Quantitative Imaging Network. *Magnetic Resonance Imaging*. 2012;30:1323-1341.

37. Sundar LKS, Yu J, Muzik O, et al. Fully Automated, Semantic Segmentation of Whole-Body ^{18}F-FDG PET/CT Images Based on Data-Centric Artificial Intelligence. *J Nucl Med*. 2022;63:1941-1948.

38. Hammers A, Allom R, Koepp MJ, et al. Three-dimensional maximum probability atlas of the human brain, with particular reference to the temporal lobe. *Human Brain Mapping*. 2003;19:224-247.

39. Otsu N. A Threshold Selection Method from Gray-Level Histograms. *IEEE Trans Syst, Man, Cybern*. 1979;9:62-66.

40. Modat M, Cash DM, Daga P, Winston GP, Duncan JS, Ourselin S. Global image registration using a symmetric block-matching approach. *J Med Imag*. 2014;1:024003.

43. Akaike H. A new look at the statistical model identification. *IEEE Trans Automat Contr*. 1974;19:716-723.

45. Leenders KL, Perani D, Lammertsma AA, et al. CEREBRAL BLOOD FLOW, BLOOD VOLUME AND OXYGEN UTILIZATION: NORMAL VALUES AND EFFECT OF AGE. *Brain*. 1990;113:27-47.

46. Berridge MS, Adler LP, Nelson AD, et al. Measurement of Human Cerebral Blood Flow with [^{15}O]Butanol and Positron Emission Tomography. *J Cereb Blood Flow Metab*. 1991;11:707-715.

47. Herzog H, Seitz RJ, Teilmann L, et al. Quantitation of Regional Cerebral Blood Flow with ^{15}O-Butanol and Positron Emission Tomography in Humans. *J Cereb Blood Flow Metab*. 1996;16:645-649.

48. Martin WR, Raichle ME. Cerebellar blood flow and metabolism in cerebral hemisphere infarction. *Ann Neurol*. 1983;14:168-176.

49. Gaillard WD, Zeffiro T, Fazilat S, DeCarli C, Theodore WH. Effect of Valproate on Cerebral Metabolism and Blood Flow: An 18F-2-Deoxyglusose and 15O Water Positron Emission Tomography Study. *Epilepsia*. 1996;37:515-521.

50. Warnert EA, Harris AD, Murphy K, et al. *In vivo* Assessment of Human Brainstem Cerebrovascular Function: A Multi-Inversion Time Pulsed Arterial Spin Labelling Study. *J Cereb Blood Flow Metab*. 2014;34:956-963.

51. Kahn D, Weiner G, Ben-Haim S, et al. Positron emission tomographic measurement of bone marrow blood flow to the pelvis and lumbar vertebrae in young normal adults [published erratum appears in Blood 1994 Nov 15;84(10):3602]. *Blood*. 1994;83:958-963.

52. Bertoldo A, Peltoniemi P, Oikonen V, Knuuti J, Nuutila P, Cobelli C. Kinetic modeling of [^{18}F]FDG in skeletal muscle by PET: a four-compartment five-rate-constant model. *American Journal of Physiology-Endocrinology and Metabolism*. 2001;281:E524-E536.

53. Taniguchi H, Yamaguchi A, Kunishima S, et al. Using the spleen for time-delay correction of the input function in measuring hepatic blood flow with oxygen-15 water by dynamic PET. *Ann Nucl Med*. 1999;13:215-221.

54. Oguro A, Taniguchi H, Koyama H, et al. Quantification of human splenic blood flow (Quantitative measurement of splenic blood flow with H2 15O and a dynamic state method: 1). *Ann Nucl Med*. 1993;7:245-250.

55. Kudomi N, Koivuviita N, Liukko KE, et al. Parametric renal blood flow imaging using [15O]H2O and PET. *Eur J Nucl Med Mol Imaging*. 2009;36:683-691.

56. Hopkins SR, Wielpütz MO, Kauczor H-U. Imaging lung perfusion. *Journal of Applied Physiology*. 2012;113:328-339.

57. Matsunaga K, Yanagawa M, Otsuka T, et al. Quantitative pulmonary blood flow measurement using 15O-H2O PET with and without tissue fraction correction: a comparison study. *EJNMMI Res*. 2017;7:102.

58. Schuster DP, Kaplan JD, Gauvain K, Welch MJ, Markham J. Measurement of regional pulmonary blood flow with PET. *J Nucl Med*. 1995;36:371-377.

59. Ibaraki M, Ito H, Shimosegawa E, et al. Cerebral Vascular Mean Transit Time in Healthy Humans: A Comparative Study with PET and Dynamic Susceptibility Contrast-Enhanced MRI. *J Cereb Blood Flow Metab*. 2007;27:404-413.

60. Biffar A, Sourbron S, Schmidt G, et al. Measurement of perfusion and permeability from dynamic contrast-enhanced MRI in normal and pathological vertebral bone marrow. *Magnetic Resonance in Med*. 2010;64:115-124.

61. Kershaw LE, Buckley DL. Precision in measurements of perfusion and microvascular permeability with T_1 -weighted dynamic contrast-enhanced MRI. *Magnetic Resonance in Med*. 2006;56:986-992.

62. Zhu B, Wang C, Gao J, Liu H, Li N, Teng Y. CT perfusion imaging of the liver and the spleen can identify severe portal hypertension. *Abdom Radiol*. 2024;49:1084-1091.

63. Sauter AW, Feldmann S, Spira D, et al. Assessment of Splenic Perfusion in Patients with Malignant Hematologic Diseases and Spleen Involvement, Liver Cirrhosis and Controls Using Volume Perfusion CT (VPCT). *Academic Radiology*. 2012;19:579-587.

64. Sourbron SP, Michaely HJ, Reiser MF, Schoenberg SO. MRI-Measurement of Perfusion and Glomerular Filtration in the Human Kidney With a Separable Compartment Model: *Investigative Radiology*. 2008;43:40-48.

65. Eikefjord E, Andersen E, Hodneland E, et al. Use of 3D DCE-MRI for the Estimation of Renal Perfusion and Glomerular Filtration Rate: An Intrasubject Comparison of FLASH and KWIC With a Comprehensive Framework for Evaluation. *American Journal of Roentgenology*. 2015;204:W273-W281.

66. Ohno Y, Hatabu H, Murase K, et al. Quantitative assessment of regional pulmonary perfusion in the entire lung using three-dimensional ultrafast dynamic contrast-enhanced magnetic resonance imaging: Preliminary experience in 40 subjects. *Magnetic Resonance Imaging*. 2004;20:353-365.

67. Giardino ND, Friedman SD, Dager SR. Anxiety, respiration, and cerebral blood flow: implications for functional brain imaging. *Comprehensive Psychiatry*. 2007;48:103-112.

68. Van Den Bergh O, Zaman J, Bresseleers J, Verhamme P, Van Diest I. Anxiety, pCO2 and cerebral blood flow. *International Journal of Psychophysiology*. 2013;89:72-77.